Korean J. Chem. Eng., 40(11), 2771-2777 (2023)
DOI: 10.1007/s11814-023-1523-y

pISSN: 0256-1115
eISSN: 1975-7220

Facile antisolvent crystallization-based synthesis of Cu/CoO nanocomposites as catalysts for the electrochemical detection of H_2O_2

Cun Liu*,‡, Jinyoung Choi*,‡, Jiyu Hyun, Suk Ho Bhang**, and Taekyung Yu*,†**

*Department of Chemical Engineering, College of Engineering, Integrated Engineering Major, Kyung Hee University, Yongin 17140, Korea
**School of Chemical Engineering, Sungkyunkwan University, Suwon, Gyeonggi 16419, Korea
(*Received 29 March 2023 • Revised 16 June 2023 • Accepted 22 June 2023*)

Abstract−To synthesize nanocomposites (NCs) comprising two different materials, a multi-step synthetic method is generally required. In this work, we report the synthesis of a heterometallic nanostructure that can be synthesized using a simple antisolvent crystallization-based method. Cu/CoO NCs composed of Cu nanoparticles and CoO nanosheets were formed by reducing mixed salt particles containing both Cu and Co precursors. The synthesized Cu/CoO NCs exhibit higher sensitivity and increased stability compared to conventional catalysts when used for the electrochemical detection of hydrogen peroxide (H_2O_2).

Keywords: Antisolvent Crystallization, Cu, CoO, Electrochemical H_2O_2 Detection, Nanocomposites

INTRODUCTION

Recently, many effectors have been devoted to the fabrication and application of nanocomposites (NCs), as their valuable activity enables the development of NCs in numerous fields, such as medical discovery, environmental engineering, and catalytic applications [1-3]. Tremendous effort has been devoted to the synthesis of heterometallic NCs because of their advantages, which include higher selectivity, higher activity, and increased chemical/physical stability compared to homometallic ones [4,5]. However, the synthesis of heterometallic NCs is limited due to their complicated synthesis steps, long reaction time, and the harsh reaction conditions [6-8]. Except that, one of the biggest problems of conventional methods for synthesis of heterostructures is that the two metal precursors start forming in different locations and grow into separate particles. To overcome this, we employed the antisolvent crystallization-based method, which can contain two metal precursors within one mixed salt nanoparticle that allows them to reside in the same location and naturally form a heterostructure during the nanoparticle growth process. Thus, we were able to easily synthesize heterostructures in a one-step process under mild conditions.

Hydrogen peroxide (H_2O_2), which is a reactive oxygen species and the simplest peroxide, has been widely used in various fields, including waste-water treatment, medical equipment, and chemical industries [9]. However, it has been reported that excess H_2O_2 can cause water pollution, soil structure damage, and the outbreak of various diseases [10,11]. Therefore, the development of reliable and convenient methods for the quantitative detection of H_2O_2 with high sensitivity and selectivity in practical applications is of great urgency. Many analytical techniques have been developed for H_2O_2 detection, including colorimetric assay [12,13], electrochemical detection [14,15], and the fluorimetry method [16,17]. Among them, the electrochemical detection technique shows great promise owing to its intrinsic advantages, such as high sensitivity, high selectivity, low cost, fast response, and simplicity [18]. Meanwhile, electrochemically active nanomaterials also play an important role in the electrochemical detection technique because of their enhanced catalytic activity and electrochemical responses for target substrate analysis [19,20]. Therefore, the development of an electrochemical H_2O_2 detection method based on nanomaterials has broad application prospects.

Among previously reported nanomaterials, Cu-based nanomaterials have emerged as the optimal catalytic material for H_2O_2 detection owing to their low cost. In addition, the redox potential of Cu^+/Cu^{2+} couples matches well with that of H_2O_2 [21,22]. For example, Bian et al. prepared a Pt-Cu octahedral alloy with controlled composition serving as a modifying agent in biosensors using a facile method, which showed substantially enhanced activity towards H_2O_2 detection [23]. Cheng et al. successfully synthesized double-shelled hollow $CuCo_2O_4$ heterostructures with a hydrothermal and calcination process. The as-prepared materials were used for the electrochemical detection of glucose and H_2O_2 and exhibited excellent performance [24]. Ma et al. constructed hollow core-shell CuS@CuSe heteromicrocubes by adopting well-defined Cu_2O microcubes and a subsequent sulfidation/selenization treatment, and the CuS@CuSe/glassy carbon electrode (GCE) displayed significantly enhanced biosensing properties for H_2O_2 reduction and dopamine (DA) oxidation [25]. In addition to Cu-based nanomaterials, Co-based catalysts with different oxidation states, shapes, and supports have also been reported for H_2O_2 sensing. For example, Ullah et al. fabricated Co_3O_4/anatase titanium dioxide nanotubes (Co_3O_4/ATNTs) by combining the two-step anodization process and the chemical bath deposition method and investigated the Co_3O_4/ATNTs for the electrochemical sensing of H_2O_2 [26]. Wu et

†To whom correspondence should be addressed.
E-mail: tkyu@khu.ac.kr
‡Authors contributed equally to this work.

al. synthesized CoS with a tremella-like nanostructure via the one-pot hydrothermal method and studied the ability of different phases of cobalt sulfides to detect glucose and H_2O_2. The sensor based on cobalt sulfides exhibited good selectivity, excellent stability, and high reproducibility [27]. Kim et al. successfully synthesized a hierarchical three-dimensional nitrogen-doped carbon nanotube-anchored bimetallic Co-Cu organic framework with the direct growth approach using a high-temperature carbonization of the bimetallic Co-Cu organic framework and found that the as-prepared nanomaterials possessed a high level of activity for both glucose and H_2O_2 sensing molecules [28].

In this work, we used the developed antisolvent crystallization-based method for synthesis of the heterometallic nanostructures composed of Cu and CoO, which were synthesized by reducing mixed salt particles containing Cu and Co precursors synthesized in the antisolvent crystallization process; the Cu/Co molar ratio in the Cu/CoO NCs was controlled by adjusting the ratio of Cu and Co precursors. In addition, the synthesized Cu/CoO NCs exhibited higher sensitivity and increased stability compared to conventional catalysts when used for the electrochemical detection of hydrogen peroxide (H_2O_2).

MATERIALS AND METHODS

1. Materials and Reagents

Copper (II) chloride ($CuCl_2$, ≥99.9%), cobalt (II) chloride ($CoCl_2$, ≥97%), sodium borohydride ($NaBH_4$, ≥98.0%), cetyltrimethylammonium bromide (CTAB), ethyl acetate (≥99.5%), ethanol (≥99.5%), Nafion solution, hydrogen peroxide (H_2O_2), sodium phosphate dibasic (Na_2HPO_4, ≥99.0%), sodium phosphate monobasic (NaH_2PO_4, ≥99.0%), hydrochloric acid (HCl, 37.0%), sodium hydroxide (NaOH, ≥98.0%), sodium chloride (NaCl, ≥99.0%), potassium chloride (KCl, ≥99.0%), ammonium chloride (NH_4Cl, ≥99.5%), sodium nitrite ($NaNO_2$, ≥99.0%), urea (≥99.0%), ascorbic acid (AA, ≥99.0%), and glucose (≥96.0%) were purchased from Sigma Aldrich (St. Louis, MO, USA). Carbon black (Vulcan XC-72) was purchased from CABOT (St. Louis, MO, USA). All chemicals were used without further purification.

2. Characterization

Transmission electron microscopy (TEM) and energy dispersive X-ray spectroscopy (EDS) images were obtained using a JEM-2100F (JEOL) microscope at 200 kV. The elemental composition of the Cu/CoO NCs was investigated using an inductively coupled plasma spectrometer (ICP, LEEMAN). Magnetic measurements were performed at room temperature using a superconducting quantum interference device-vibrating sample magnetometer (SQUID-VSM QM02). X-ray diffraction (XRD) patterns were recorded using a D8 Advance X-ray diffractometer operated at 35 kV and 35 mA. X-ray photoelectron spectroscopy (XPS) spectra were obtained using a PHI 5000 VersaProbe (ULVAC PHI, Chigasaki, Kanagawa, Japan). Thermogravimetric analysis (TGA) curves were obtained using a Seiko Exstar 6000 (TG/DTA6100). The electrocatalytic activity of the Cu/CoO NCs was evaluated using a CHI 760E electrochemical workstation (CH Instruments).

3. Synthesis of Cu/CoO NCs

First, 12 mg of $CuCl_2$, 26 mg of $CoCl_2$, and 10 mg of CTAB were dissolved in 3 mL of deionized (DI) water and preheated at 70 °C for 30 min. Next, 6 mL of ethyl acetate was injected into the mixture, which was heated at 70 °C for 30 min and stirred at 800 rpm. Once a cloudy solution was formed, 3 mL of aqueous $NaBH_4$ (11.4 mg) was injected into the mixture, heated at 70 °C for 10 min, and stirred at 800 rpm. After the reaction, the products were collected via centrifugation (9,000 rpm, 10 min, 3 cycles) and redispersed in DI water.

4. Preparation of Vulcan XC-72 Solution

First, 500 mg of Vulcan XC-72 was dissolved in 50 mL of deionized (DI) water and sonicated for 20 min to disperse. Next, 30 mL of HCl was injected into the mixture and stirred for 12 h at room temperature. The final product was collected by centrifugation (13,000 rpm, 15 min, 3 cycles) and re-dispersed in 100 mL of ethanol (concentration of 5 mg/mL).

5. Preparation of Cu/CoO Supported on Carbon

After dispersing the Cu/CoO NCs in 17.6 mL of ethanol, 2.4 mL of the ethanol solution containing Vulcan XC-72 was injected into the mixture and heated at 75 °C for 1 h. The carbon-supported catalysts were collected by centrifugation and redispersed in 1 mL of ethanol [29].

6. Preparation of Phosphate Buffered Saline (PBS)

In 100 mL of DI water, 1.42 g of Na_2HPO_4 and 1.2 g of NaH_2PO_4 were dissolved. Then, 28.85 mL of Na_2HPO_4 and 21.15 mL of NaH_2PO_4 solutions were mixed. The pH value of the PBS buffer solution was adjusted using HCl and NaOH solutions.

7. Electrochemical Measurements

The electrochemical response was evaluated using a three-electrode cell system consisting of a reference electrode (saturated Ag/AgCl electrode), a counter electrode (graphite rod), and a working electrode (GCE with a working area of 0.07 cm^2). The catalyst ink was prepared as follows: a certain amount of the Cu/CoO catalyst and 45 μL of the Nafion solution were added to 555 μL of ethanol and sonicated for 15 min to form a homogeneous solution. The as-prepared catalyst ink was then dropped on the working electrode and left to dry at room temperature for 15 min. All electrochemical measurements were conducted in 50 mL of 0.1 M PBS (pH=7), and the PBS solution was purged with nitrogen to obtain a N_2-saturated atmosphere.

RESULTS AND DISCUSSION

1. Characterization of Heterometallic Structure Cu/CoO NCs

The Cu/CoO NCs were synthesized using the antisolvent crystallization-based synthetic method, as shown in Fig. 1. Cu-Co mixed salt nanoparticles (NPs) were synthesized by mixing an aqueous solution containing Cu and Co precursors with ethyl acetate as the antisolvent. Fig. S1 shows typical TEM and EDS mapping images of salt NPs, depicting the formation of 117.5 nm-sized quasi-spherical particles composed of Co, Cu, and Cl. After reduction with $NaBH_4$, the pink cloudy-colored solution rapidly turns black, indicating that the salt NPs were converted to metallic nanomaterials. TEM and EDS mapping images (Fig. 2 and Fig. S2, respectively) show the formation of composites approximately 2 μm in size composed of CoO nanosheets and Cu nanoparticles with an average size of 32.6 nm. The XRD pattern of the Cu/CoO NCs in Fig. 3 shows

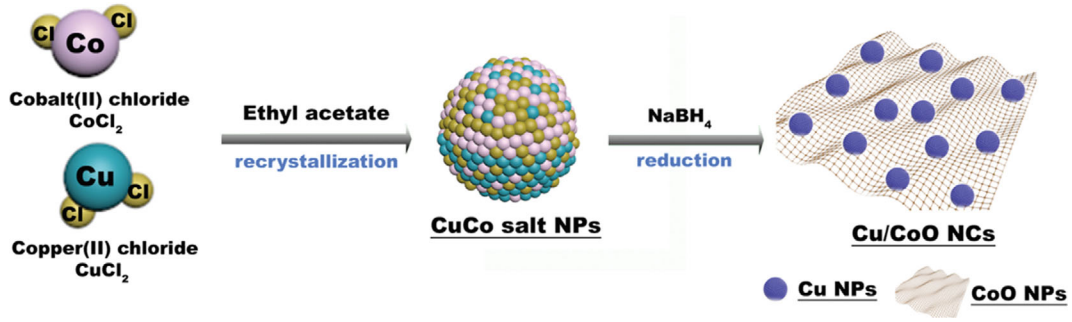

Fig. 1. Schematic illustration of the synthesis process of Cu/CoO NCs.

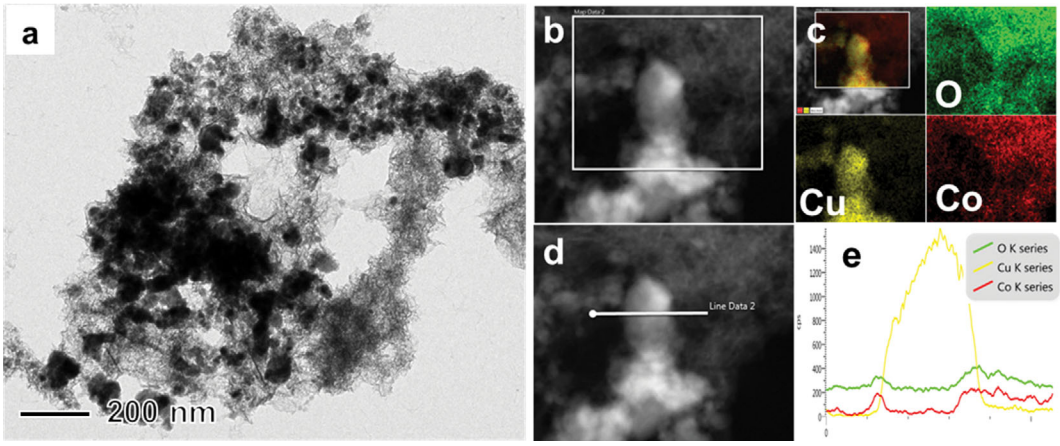

Fig. 2. (a) TEM image and (b-d) corresponding EDS mapping images of the Cu/CoO NCs. (e) EDS line scan graph of the Cu/CoO NCs.

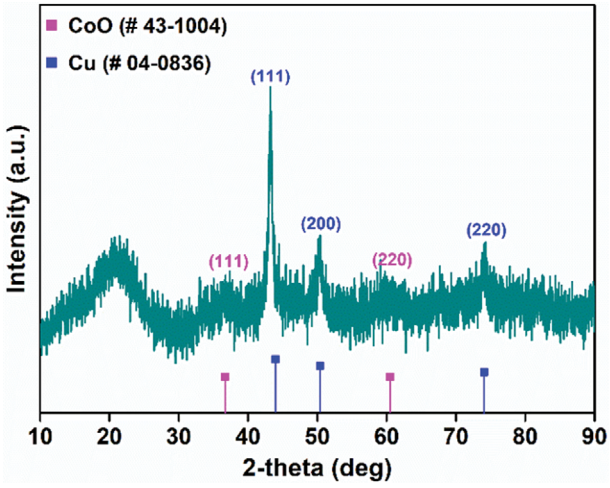

Fig. 3. XRD patterns of the Cu/CoO NCs.

diffraction peaks at 43.3°, 50.4°, and 74.1°, which correspond to (111), (200), and (220), respectively, indicating the presence of metallic Cu (JCPDS #04-0836). In addition, diffraction peaks were also observed at 36.5° and 61.5°, which correspond to (111) and (220), respectively, indicating the presence of metallic CoO (JCPDS #43-1004). The high-resolution TEM (HRTEM) analysis indicates the presence of two lattices in the NCs, which match well with Cu and CoO [30,31]. To obtain more detailed information of the structure, XPS analysis was performed (Fig. 4). As shown in Fig. 4(a), the Cu 2p XPS spectra could be deconvoluted into two prominent peaks at 932.4 eV and 954.4 eV, both of which correspond to Cu $2p_{3/2}$ of the zero-valent [32]. Meanwhile, the Co 2p XPS spectra exhibited two major peaks corresponding to Co $2p_{3/2}$ (780.0 eV) and Co $2p_{1/2}$ (795.9 eV) of CoO, both of which have satellite peaks at the corresponding binding energies, which represent the oxidation state of cobalt (Fig. 4(b)) [33]. These results are consistent with that of the XRD analysis. Therefore, it can be deduced that the as-prepared NCs were composed of metallic Cu and CoO. The Cu/Co atomic ratio in the Cu/CoO NCs was calculated according to the ICP results, where it was revealed that the Cu/Co ratio can be easily controlled by adjusting the Cu/Co precursor ratio (Table S1). Interestingly, the synthesized NCs exhibited a superparamagnetic nature with a saturation magnetization (G_s) value of 11.171 emu g^{-1} (Fig. S5), which can be attributed to the exchange coupling that occurred at the Cu-CoO interface where the magnetic moments of CoO influence the behavior of neighboring Cu atoms. This interaction can result in a modification of the magnetic properties, potentially leading to a stronger overall magnetism compared to the individual components [34].

2. Electrochemical H_2O_2 Detection

Previous research conducted on H_2O_2 detection using Cu- and Co-based nanomaterials found that a combination of Cu and Co could effectively enhance the resolution limitation, resulting in a sensor with high accuracy [35-37]. To verify the catalytic activity

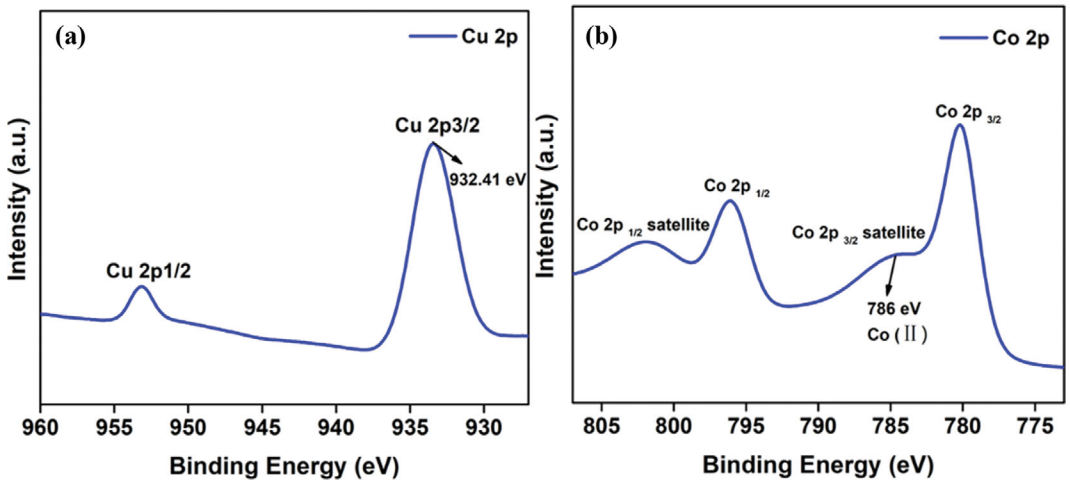

Fig. 4. XPS spectra of (a) Cu 2p and (b) Co 2p in the Cu/CoO NCs.

of Cu/CoO catalysts for H_2O_2 detection, electrochemical cyclic voltammetry (CV) measurements were first performed in 0.1 M PBS with and without H_2O_2. As shown in Fig. S6(a), a reduction peak was observed at −0.135 V (vs. Ag/AgCl) and a weak oxidation peak at −0.03 V without H_2O_2. This can be attributed to the redox reaction of Cu/CoO NCs. The intensity of the reduction peak increased significantly after the addition of 1 mM of H_2O_2, indicating that it was involved in the reaction. The as-prepared Cu/CoO catalyst is catalytically active. Notably, the electrochemical surface area (ESCA) is important for the electrochemical detection of trace amounts of chemical species [38,39]. The ECSA of the Cu/CoO (0.07 mF cm^{-2}) is very small (Fig. S7(a), (d)), indicating that there was limited interfacial charge transfer, resulting in decreased detection sensitivity and a low resolution. The double-layer capacitance (Cdl) was in proportion to the ESCA of the electrode and was obtained by plotting the ΔJ/2 against the scan rate, where ΔJ denotes the difference between anodic and cathodic currents at the same potential [40]. To improve the interfacial charge transfer of the Cu/CoO NCs, we tried to support the Cu/CoO NCs on the Vulcan XC-72 to increase the conductivity [41]. Fig. S8 shows the TEM image and elemental distribution of the Cu/CoO supported on carbon, indicating the Cu/CoO NCs were successfully dispersed on the carbon. The TGA results show that the amount of Cu/CoO on the carbon was 21 wt% (Fig. S9); therefore, it can be deduced that carbon particles without catalysts had no significant catalytic activity for H_2O_2 detection (Figs. S6(b), S7(b), and S7(d)). The CV measurements of the Cu/CoO catalyst supported on carbon in the absence and presence of H_2O_2 show that the reduction peak increased after the addition of H_2O_2, and the ECSA increased to 1.85 mF cm^{-2}, which is much larger than that of the bare Cu/CoO catalyst (Figs. S6(c), S7(c), and S7(d)). Therefore, the Cu/CoO supported on carbon was used as the catalyst for further electrochemical experiments in this study.

To obtain the optimal detection performance, optimization of the applied potential, catalyst amount, and pH was necessary. The applied potential was optimized via amperometry tests with the successive addition of H_2O_2 at different potentials (Fig. S10(a)). The electrochemical response increased from −0.1 V to −0.2 V before decreasing. Further, the calibration curve indicated that the current response at −0.2 V had the largest slope (Fig. S10(b)). Through control experiments of the catalyst amount and pH value of the solution, we confirmed that the optimal conditions were 15 μg of the catalyst and a pH value of 7 (Fig. S11 and S12).

Under optimized conditions, the current response of the Cu/CoO catalyst with successive additions of H_2O_2 at −0.2 V was measured every 60 s. As shown in Fig. 5(a), the Cu/CoO catalyst had a quick response time after the addition of H_2O_2. The calibration curve between the H_2O_2 concentration and current response is shown in Fig. 5(b)-(d). The linear relationship can be expressed as j (mA cm^{-2})=−0.0463C (mM)−0.00259 (R^2=0.99966) in the range of 10 to 100 μM, and j (mA cm^{-2})=−0.0277C (mM)−0.00441 (R^2=0.99879) in the range of 100 to 1,000 μM, where j is the current density, C is the H_2O_2 concentration, and the slope is the sensitivity. The sensitivity was 46.3 μA mM^{-1} cm^{-2} and 27.7 μA mM^{-1} cm^{-2} from 10 to 100 μM and 100 to 1,000 μM, respectively. The limit of detection (LOD) was 1.85 μM, as calculated using the following equation: $3\sigma/N$, where σ is the standard deviation of the background current and N is the sensitivity [42]. In addition, we also performed a control experiment using pure CoO nanosheets and Cu nanoparticles as the catalyst for H_2O_2 detection, as shown in Fig. S13 and Fig. S14. The limit of detection was 4.04 μM for CoO nanosheets and 8.5 μM for Cu nanoparticles, respectively, which indicated the importance of the Cu/CoO heterostructure. In addition, compared with previous reported catalysts for H_2O_2 electrochemical detection (Table S2), the as-prepared Cu/CoO catalyst also exhibited enhanced catalytic activity and increased sensitivity [25,43-50].

Selectivity and stability are also important parameters in the practical use of catalytic sensors to sensor. To analyze the selectivity of the Cu/CoO catalyst, NaCl, KCl, NH_4Cl, $NaNO_2$, urea, AA, and glucose were chosen as the controls and successively added to 0.1 M PBS at −0.2 V (vs. Ag/AgCl). As shown in Fig. 6(a), the catalyst showed a negligible response to the controls compared with H_2O_2, indicating the excellent selectivity of the Cu/CoO catalyst for H_2O_2 detection. In addition, the stability of the catalyst was investigated by recording the current signal after the addition of the same concentration of H_2O_2 daily for 7 d. Under the same catalytic condi-

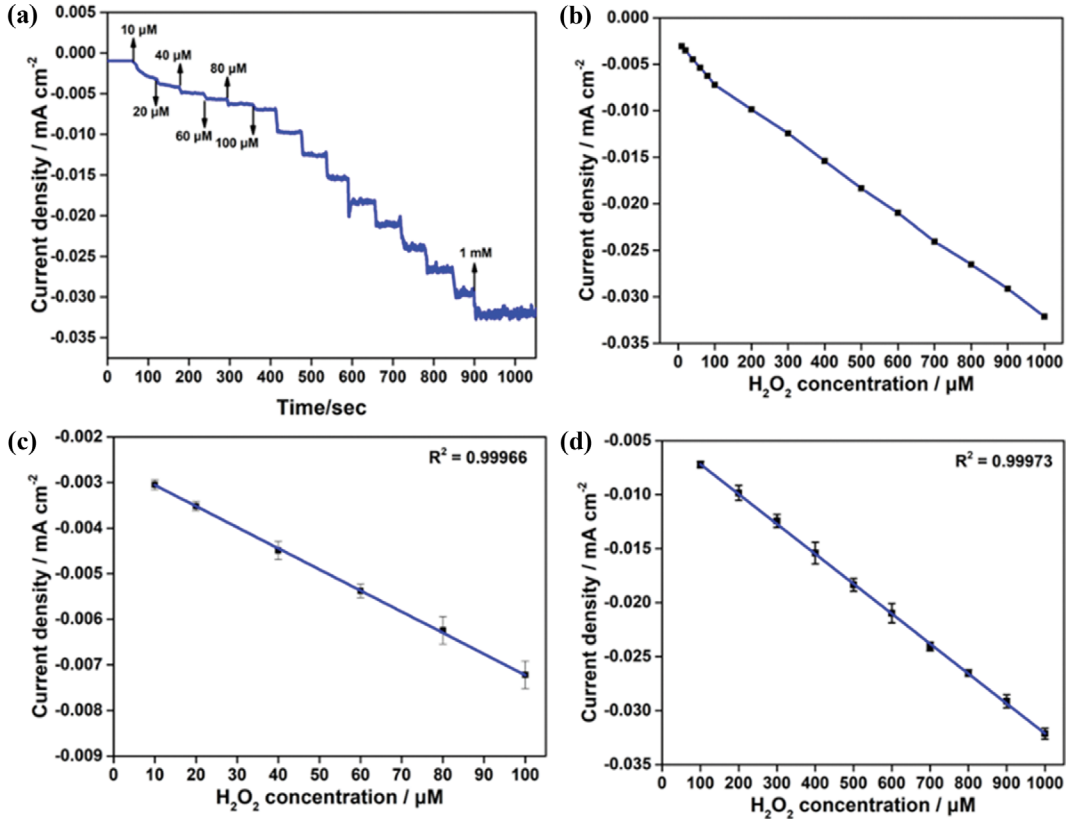

Fig. 5. (a) Amperometric responses of the Cu/CoO catalyst with successive additions of H_2O_2 in 0.1 M PBS solution (pH=7) at −0.2 V (vs. Ag/AgCl). (b) Linear relationship between the current density and H_2O_2 concentration of Cu/CoO catalyst at −0.2 V in 0.1 M PBS solution. ((c) and (d)) Linear relationship between the current density and H_2O_2 concentration in the range of 10 to 100 μM and 100 to 1 mM, respectively.

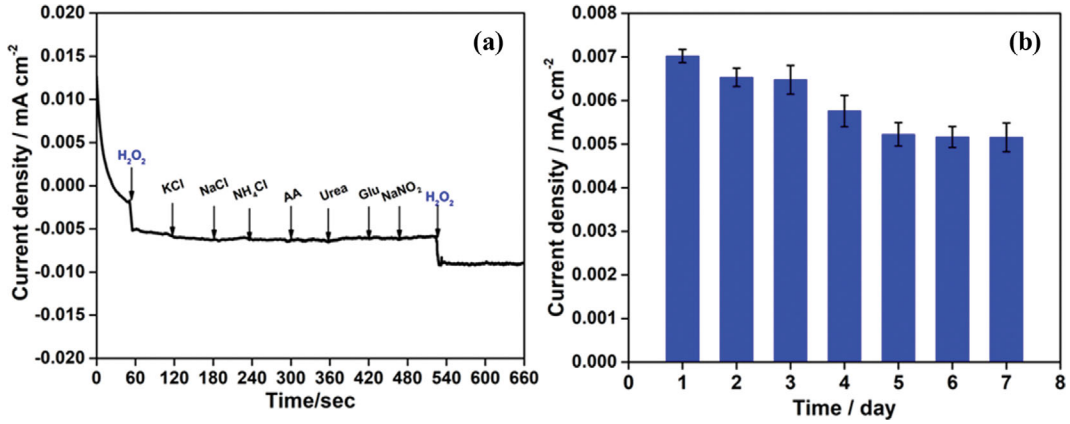

Fig. 6. (a) Amperometric response of the Cu/CoO catalyst with the addition of H_2O_2, NaCl, KCl, NH_4Cl, urea, AA, glucose, and $NaNO_2$ at −0.2 V (vs. Ag/AgCl) in 0.1 M PBS solution. (b) Amperometric responses of the Cu/CoO catalyst with the injection of 100 μM of H_2O_2 at −0.2 V in 0.1 M PBS solution (pH=7); measurements were recorded daily for 7 d.

tions, the measured current density only decreased by 26.7% after 7 d (Fig. 6(b)), indicating that the as-prepared Cu/CoO had good stability.

CONCLUSION

We have demonstrated that heterometallic nanostructures can be easily synthesized using an antisolvent crystallization-based method. Nanocomposites composed of Cu nanoparticles and CoO nanosheets were synthesized by reducing mixed salt particles containing Cu and Co precursors. The synthesized Cu/CoO NCs exhibit excellent H_2O_2 detection performance. We expect that the antisolvent crystallization-based method can be used practically in the field of heterometallic nanostructure synthesis, including bimodal,

core-shell, and dendrite-forming alloy structured nanoparticles.

ACKNOWLEDGEMENTS

This research was funded by the National Research Foundation of Korea (NRF) under grants listed as NRF-2021R1A5A6002853 and NRF-2020R1A2C1003885. This work was also supported by the Korea Institute for Advancement of Technology (KIAT) and the Ministry of Trade, Industry & Energy (MOTIE) of the Republic of Korea (No. P0017363).

AUTHOR CONTRIBUTIONS

Cun Liu: Conceptualization, synthesis, characterization, catalytic activity assay, data analysis and writing-original draft preparation. Jinyoung Choi: synthesis, characterization. Taekyung Yu: Supervision, methodology, further data analysis, writing, review.

DECLARATION OF COMPETING INTEREST

The authors declare that they have no known competing financial interests or personal relationships that could have appeared to influence the work reported in this paper.

SUPPORTING INFORMATION

Additional information as noted in the text. This information is available via the Internet at http://www.springer.com/chemistry/journal/11814.

REFERENCES

1. M. Nurdin, M. Maulidiyah, A. H. Watoni, A. Armawansa, L. O. A. Salim, Z. Arham and A. A. Umar, *Korean J. Chem. Eng.*, **39**, 209 (2022).
2. T. Thiyagarajan, V. Deivasigamani, M. Raj, C. Joseph, T. Dheivasigamani, B. Palanivel and M. Shkir, *Korean J. Chem. Eng.*, **38**, 952 (2021).
3. C. V. Khedkar, A. S. Vedpathak, A. V. Dhotre, K. D. Daware, Y. D. Kolekar, S. D. Sartale and S. I. Patil, *Chem. Phys. Impact*, **6**, 100153 (2023).
4. L. Wang, Y. Nemoto and Y. Yamauchi, *Am. Chem. Soc.*, **133**, 9674 (2011).
5. M. M. Nejadian, N. M. Mahmoodi, C. Ghotbi and F. Khorasheh, *Korean J. Chem. Eng.*, **39**, 2713 (2022).
6. L. X. Zhou, Y. Y. Yang, H. L. Zhu and Y. Q. Zheng, *Chem. Pap.*, **75**, 1795 (2021).
7. S. Tabassum, M. Usman, H. A. Al-Lohedan, M. M. Abdullah, M. A. Ghanem, M. S. Al-Sharif and M. S. Ali, *RSC Adv.*, **10**, 13126 (2020).
8. A. Z. Warsi, O. K. Hussien, A. Iftikhar, F. Aziz, D. Alhashmialameer, S. F. Mahmoud and D. I. Saleh, *Ceram. Int.*, **48**, 19056 (2022).
9. H. T. T. Vu, V. L. N. Vo and Y. M. Chung, *Korean J. Chem. Eng.*, **38**, 1139 (2021).
10. M. R. Karim, T. H. Han, S. Y. Sawant, J. J. Shim, M. Y. Lee, W. K. Kim and M. H. Cho, *Korean J. Chem. Eng.*, **37**, 1241 (2020).
11. W. Chen, H. Fan, K. Balakrishnan, Y. Wang, H. Sun, Y. Fan and X. Peng, *J. Med. Chem.*, **61**, 9132 (2018).
12. J. Lu, H. Zhang, S. Li, S. Guo, L. Shen, T. Zhou and Y. Zhang, *Inorg. Chem.*, **59**, 3152 (2020).
13. C. Liu, S. H. Im and T. Yu, *Catalysts*, **11**, 343 (2021).
14. K. Dhara and D. R. Mahapatra, *J. Mater. Sci.*, **54**, 12319 (2019).
15. S. Y. Guvenc, A. Cebi, E. Can-Güven, A. Demir, F. Ghanbari and G. Varank, *Korean J. Chem. Eng.*, **39**, 2555 (2022).
16. J. Tang, F. Li, C. Liu, J. Shu, J. Yue, B. Xu and W. Jiang, *Anal. Chim. Acta*, **1214**, 339939 (2022).
17. D. J. Zheng, Y. S. Yang and H. L. Zhu, *TrAC Trends Anal. Chem.*, **118**, 625 (2019).
18. W. Li, Y. Yang, C. Ma, Y. Song, C. Hong and X. Qiao, *J. Mater. Sci.*, **55**, 13980 (2020).
19. Y. Li, W. Zhu, Q. Kang, L. Yang, Y. Zhang, Y. Wang and Q. Wei, *ACS Appl. Mater. Interfaces*, **10**, 38791 (2018).
20. Y. Li, L. Liu, X. Liu, Y. Ren, K. Xu, N. Zhang and Q. Wei, *Biosens. Bioelectron.*, **163**, 112280 (2020).
21. F. Li, J. Feng, Z. Gao, L. Shi, D. Wu, B. Du and Q. Wei, *ACS Appl. Mater. Interfaces*, **11**, 8945 (2019).
22. Y. Dai, X. Zhu, H. Liu, Y. Lin, W. Sun, Y. Sun and Q. Wei, *Biosens. Bioelectron.*, **112**, 143 (2018).
23. T. Bian, H. Liu, B. Sun, B. Xiao, Y. Jiang, C. Jin and D. Yang, *J. Alloys Compd.*, **788**, 1334 (2019).
24. D. Cheng, T. Wang, G. Zhang, H. Wu and H. Mei, *J. Alloys Compd.*, **819**, 153014 (2020).
25. X. Ma, K. L. Tang, K. Lu, B. Yuan, W. Shi, Y. Li and W. Zhao, *Sens. Actuators, B*, **359**, 131592 (2022).
26. R. Ullah, M. A. Rasheed, S. Abbas, K. U. Rehman, A. Shah, K. Ullah and G. Ali, *Curr. Appl. Phys.*, **38**, 40 (2022).
27. W. Wu, B. Yu, H. Wu, S. Wang, Q. Xia and Y. Ding, *Mater. Sci. Eng. C*, **70**, 430 (2017).
28. S. E. Kim and A. Muthurasu, *Electroanalysis*, **33**, 1333 (2021).
29. X. Xiao, E. Jung, S. Yoo, T. Lim, J. Kim and T. Yu, *Catalysts*, **10**, 1133 (2020).
30. R. P. Ye, L. Lin, Q. Li, Z. Zhou, T. Wang, C. K. Russell and M. Fan, *Catal. Sci. Technol.*, **8**, 3428 (2018).
31. W. Xu, Z. Wang, L. Shang, H. Zhang, A. M. Al-Enizi, Y. Tang and G. Zheng, *Chem. Commun.*, **54**, 3867 (2018).
32. W. Sang, C. Wang, X. Zhang, X. Yu, C. Yu, J. Zhao and L. Li, *Int. J. Hydrogen Energy*, **42**, 30691 (2017).
33. H. P. R. Kannapu, V. Vaddeboina and Y. K. Park, *Catal. Today*, **397**, 28 (2022).
34. Q. Feng, W. Dizayee, X. L. Li, D. S. Score, J. R. Neal, A. J. Behan, A. Mokhtari, M. S. Alshammari, M. S. Al-Qahtani, H. J. Blythe, R. W. Chantrell, S. M. Heald, X. H. Xu, A. M. Fox and G. A. Gehring, *New J. Phys.* **18**, 113040 (2016).
35. A. Ngamaroonchote, Y. Sanguansap, T. Wutikhun and K. Karn-Orachai, *Microchim. Acta*, **187**, 1 (2020).
36. Z. M. Sheng, H. Huang, R. L. Niu, Z. W. Han and R. P. Jia, *Sens. Actuators, B*, **305**, 127550 (2020).
37. M. Liu, M. An, J. Xu, T. Liu, L. Wang, Y. Liu and J. Zhang, *Appl. Surf. Sci.*, **542**, 148699 (2021).
38. B. Li, L. H. Liu, X. F. Zhang, Y. Gao, Z. P. Deng, L. H. Huo and S. Gao, *Anal. Chim. Acta*, **1143**, 73 (2021).
39. C. Zhao, H. Zhang and J. Zheng, *J. Electroanal. Chem.*, **784**, 55 (2017).
40. F. Wang, K. Zhang, S. Li, Q. Zha and Y. Ni, *ACS Sustain. Chem.*

Eng., **10**, 10383 (2022).
41. D. Pantea, H. Darmstadt, S. Kaliaguine and C. Roy, *Appl. Surf. Sci.*, **217**, 181 (2003).
42. A. Shrivastava and V. B. Gupta, *Chron. Young Sci.*, **2**, 21 (2011).
43. B. Patella, M. Buscetta, S. Di Vincenzo, M. Ferraro, G. Aiello, C. Sunseri and C. Cipollina, *Sens. Actuators, B*, **327**, 128901 (2021).
44. M. A. Rashed, M. Faisal, F. A. Harraz, M. Jalalah, M. Alsaiari and S. A. Alsareii, *J. Electrochem. Soc.*, **168**, 027512 (2021).
45. L. Kong, Z. Ren, N. Zheng, S. Du, J. Wu, J. Tang and H. Fu, *Nano Res.*, **8**, 469 (2015).
46. N. Han, S. Hu, L. Zhang, S. Yi, Z. Zhang, Y. Wang and Y. Gao, *Appl. Surf. Sci.*, **576**, 151879 (2022).
47. L. Zhang, F. Yuan, X. Zhang and L. Yang, *Chem. Cent. J.*, **5**, 1 (2011).
48. C. Y. Lin and C. T. Chang, *Sens. Actuators B*, **220**, 695 (2015).
49. C. Santhosh, R. Deivasegamani, R. Nivetha, A. Bhatnagar, S. K. Jeong and A. N. Grace, *Microchim. Acta*, **184**, 3223 (2017).
50. H. Xia, J. Li, L. Ma, Q. Liu and J. Wang, *J. Alloys Compd.*, **739**, 764 (2018).

Supporting Information

Facile antisolvent crystallization-based synthesis of Cu/CoO nanocomposites as catalysts for the electrochemical detection of H_2O_2

Cun Liu*,‡, Jinyoung Choi*,‡, Jiyu Hyun, Suk Ho Bhang**, and Taekyung Yu*,†**

*Department of Chemical Engineering, College of Engineering, Integrated Engineering Major, Kyung Hee University, Yongin 17140, Korea
**School of Chemical Engineering, Sungkyunkwan University, Suwon, Gyeonggi 16419, Korea
(*Received 29 March 2023 • Revised 16 June 2023 • Accepted 22 June 2023*)

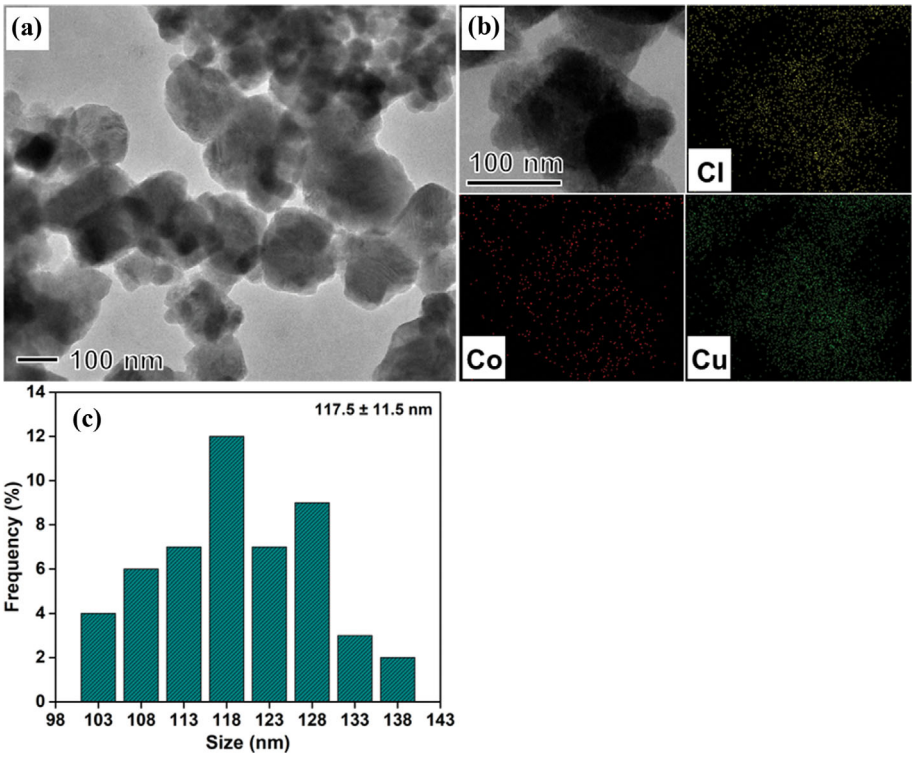

Fig. S1. (a) TEM images, (b) the corresponding EDS mapping images and (c) size distribution of mixed salt nanoparticles.

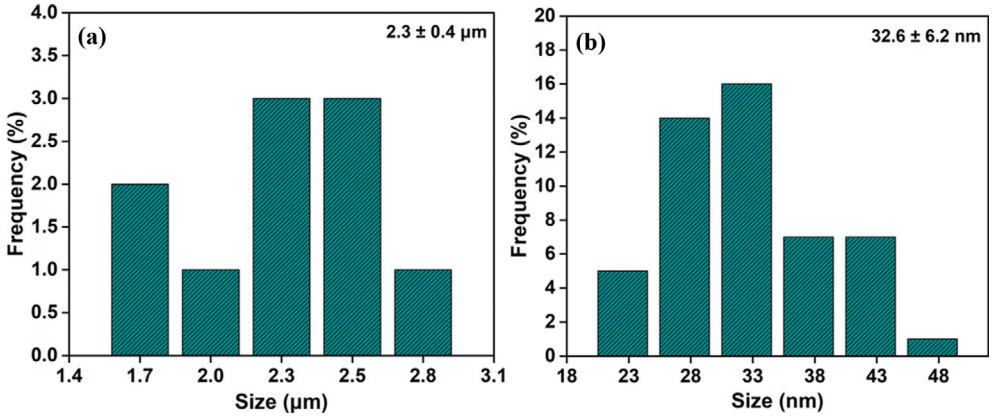

Fig. S2. Size distribution of (a) Cu/CoO NCs and (b) Cu nanoparticles.

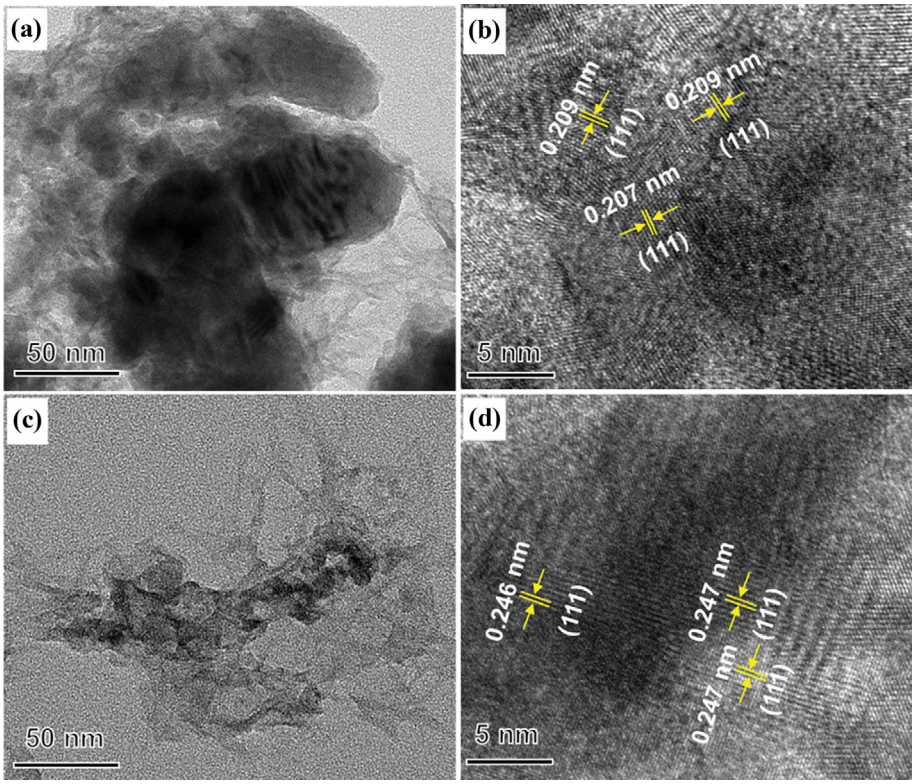

Fig. S3. TEM and HRTEM images of ((a) and (b)) Cu and ((c) and (d)) CoO in the Cu/CoO NCs.

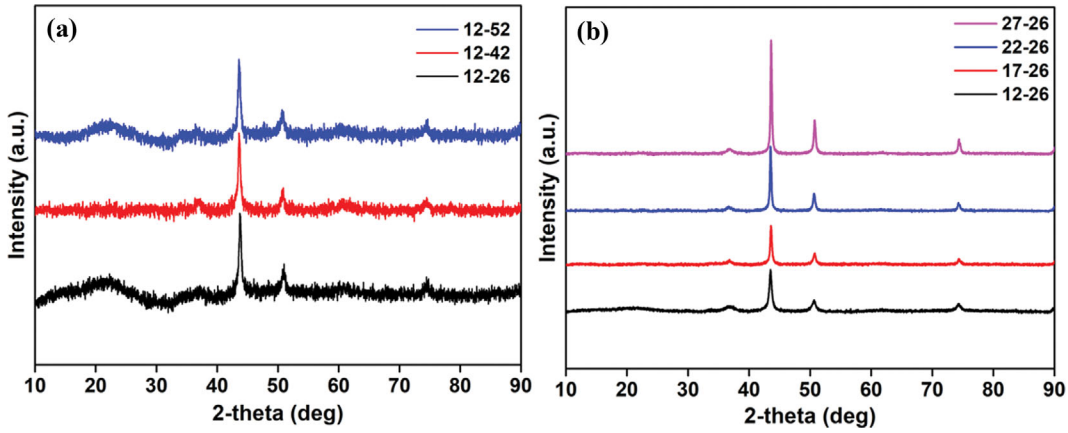

Fig. S4. XRD pattern of the Cu/CoO NCs synthesized under different (a) Co and (b) Cu precursor amounts.

Table S1. ICP data of the Cu/CoO NCs with different amount of Cu and Co precursors

Sample	Cu (mg/mL)	Co (mg/mL)	Cu/Co molar ratio
12-26	9.17	8.78	0.97/1
12-42	6.01	5.46	1.02/1
12-52	9.34	7.7	1.13/1
17-26	17.5	4.84	3.35/1
22-26	16.6	2.19	7.03/1
27-26	14.1	0.989	13.22/1

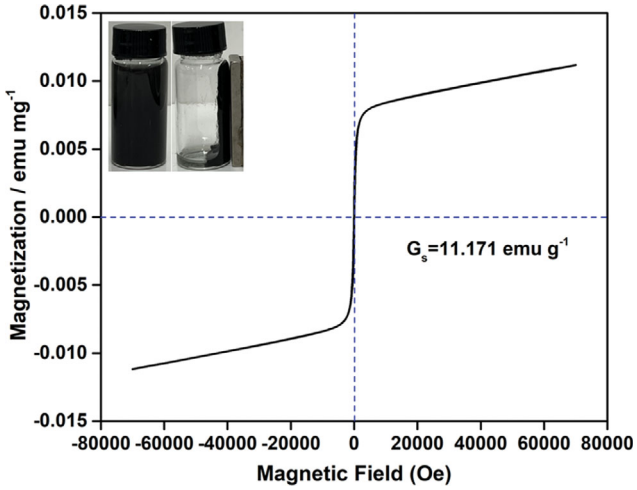

Fig. S5. Magnetization curve of the Cu/CoO NCs at room temperature. Inset is photographs before and after magnetic separation in the solution.

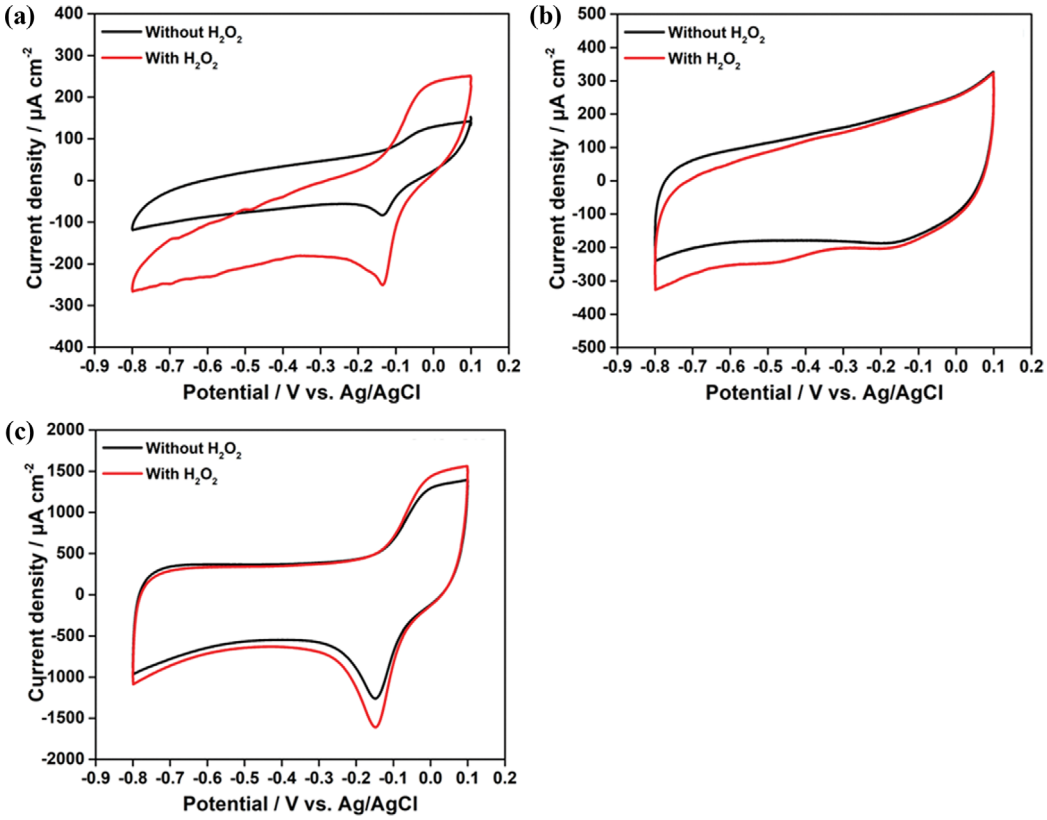

Fig. S6. CV curves of (a) the bare Cu/CoO NCs, (b) Vulcan XC-72 carbon, and (c) Cu/CoO supported on the carbon in presence and absence of H_2O_2 (1 mM).

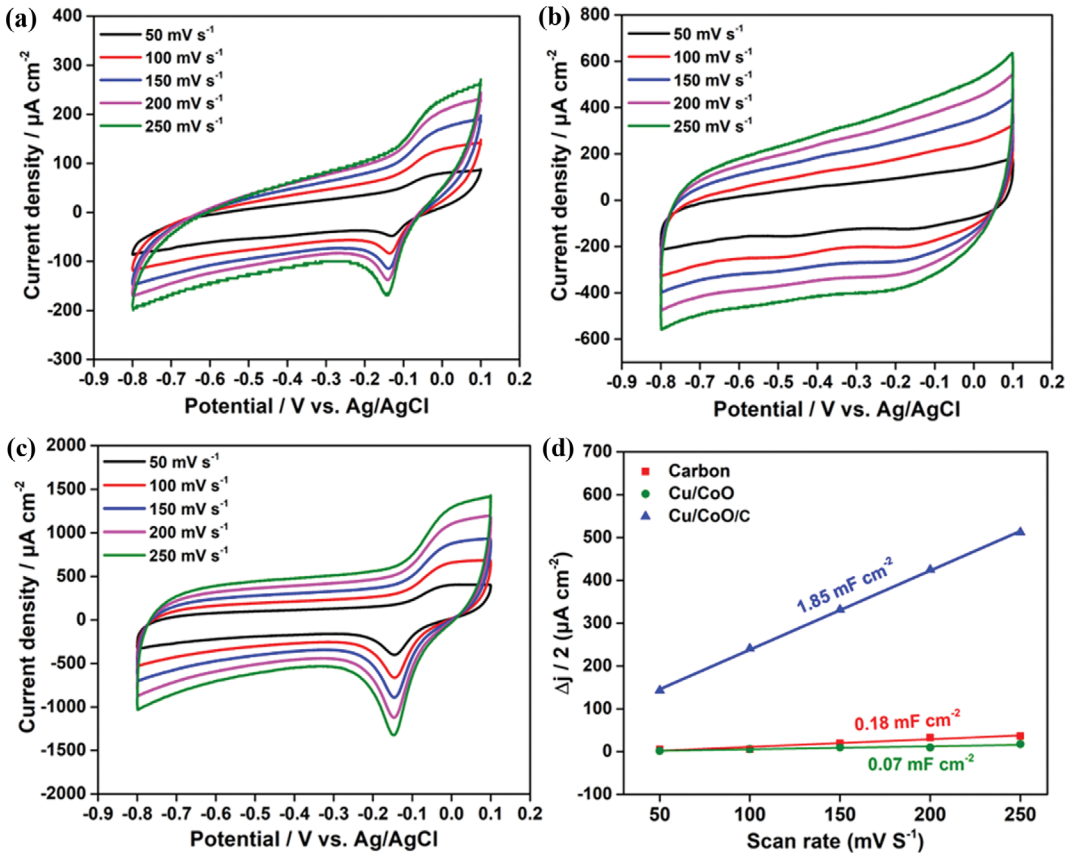

Fig. S7. (a)-(c) CV curves with five different scan rates of (a) the bare Cu/CoO NCs, (b) Vulcan XC-72 carbon, and (c) Cu/CoO supported on carbon (Cu/CoO/C), respectively. (d) Capacitive currents plotted as a function of scan rate at 0.4 V vs. Ag/AgCl.

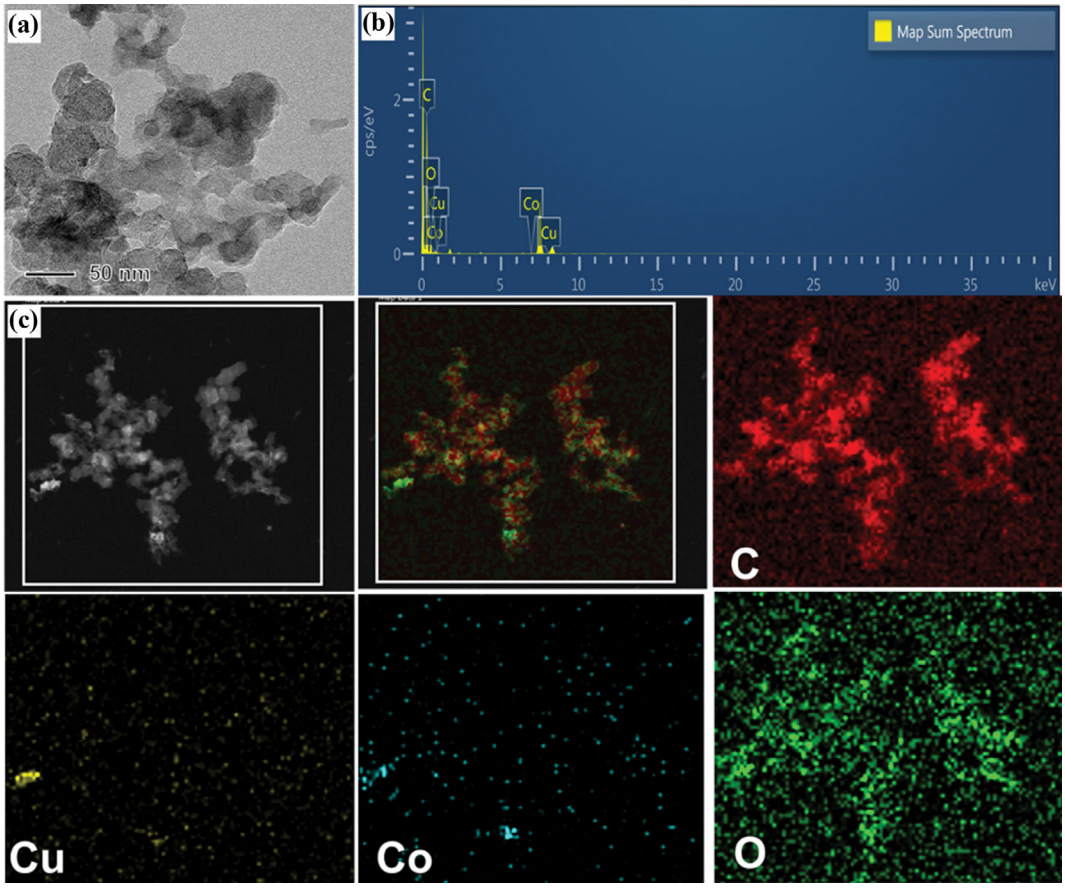

Fig. S8. (a) TEM image, ((b) and (c)) EDS mapping results of the Cu/CoO supported on the carbon.

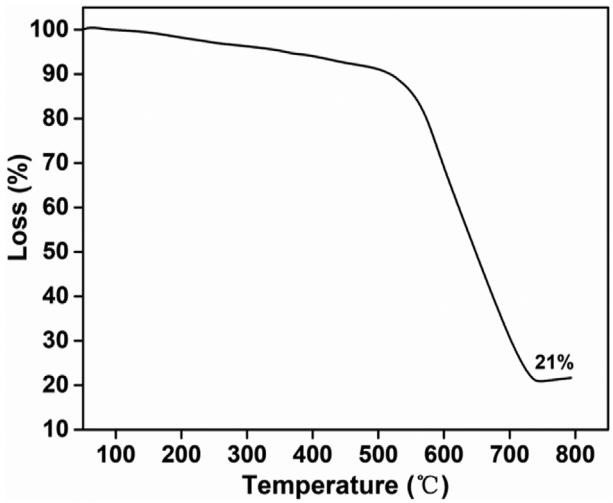

Fig. S9. The TGA graph of the Cu/CoO supported on carbon.

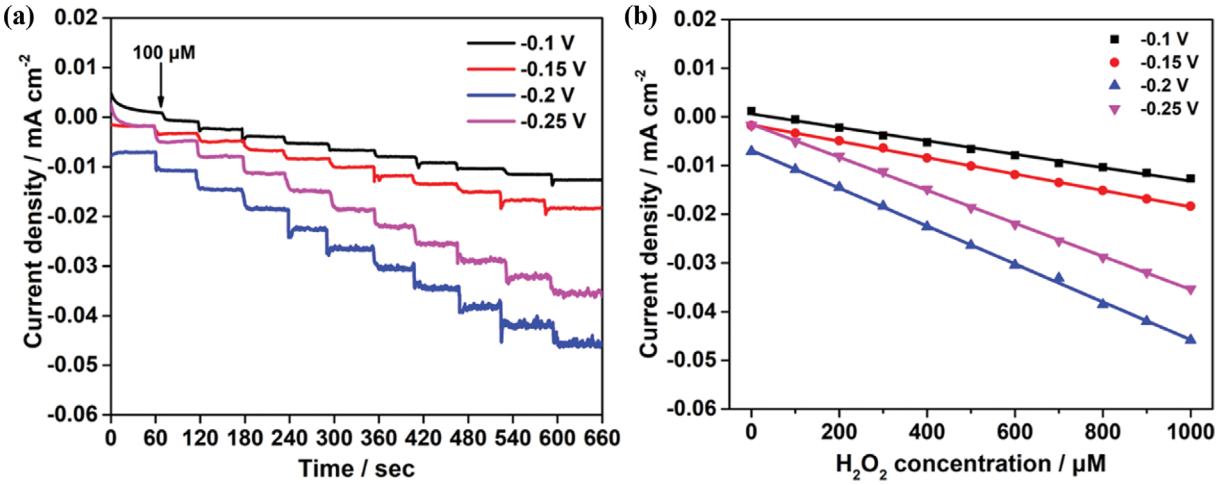

Fig. S10. (a) Amperometric responses of the Cu/CoO at different potentials in 0.1 M PBS solution with the successive addition of 100 μM H_2O_2. (b) The relationship between response current density and H_2O_2 concentration of the Cu/CoO/C at various potentials in 0.1 M PBS solution.

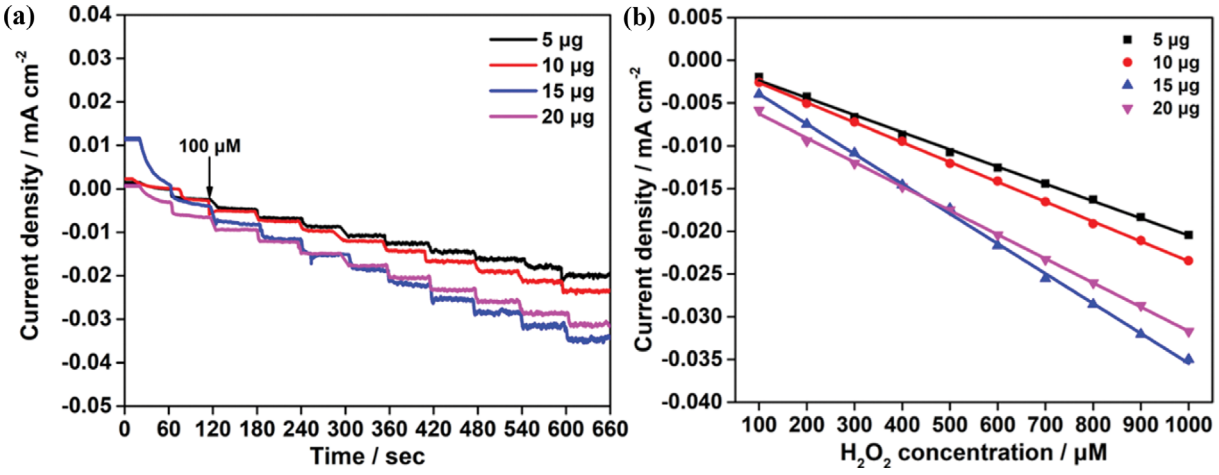

Fig. S11. (a) Amperometric responses of the Cu/CoO at different loading amount in 0.1 M PBS solution with the successive addition of 100 μM H_2O_2. (b) The relationship between response current density and H_2O_2 concentration of the Cu/CoO at various loading amount in 0.1 M PBS solution.

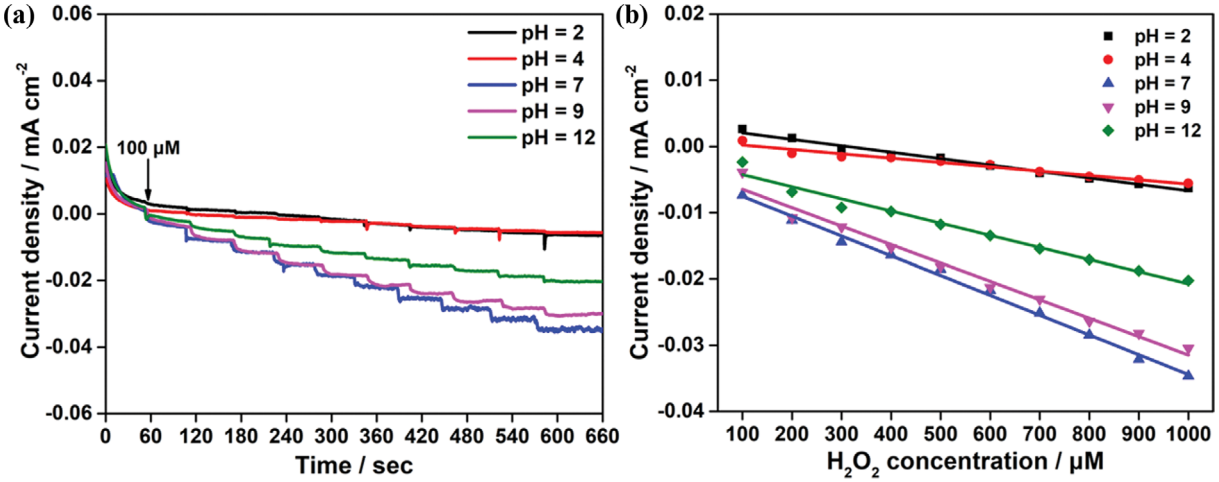

Fig. S12. (a) Amperometric responses of the Cu/CoO in 0.1 M PBS solution with different pH with the successive addition of 100 μM H_2O_2. (b) The relationship between response current density and H_2O_2. concentration of the Cu/CoO at various pH in 0.1 M PBS solution.

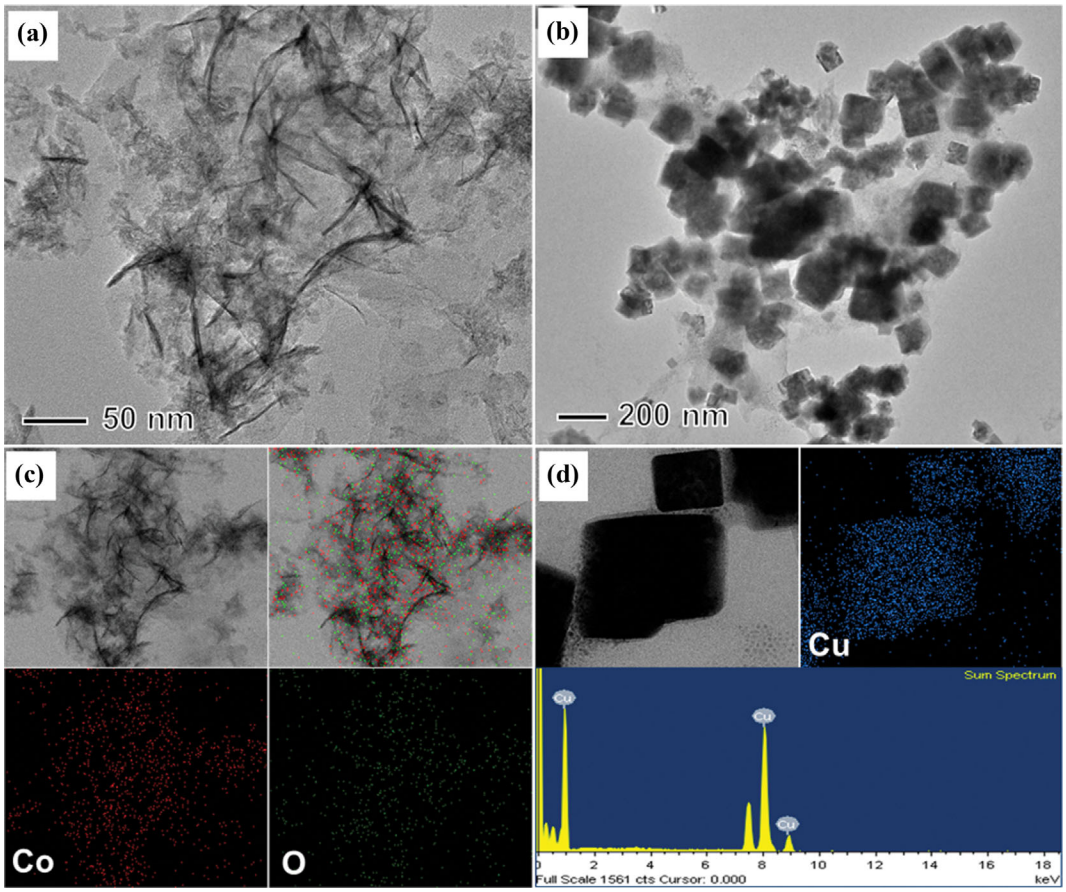

Fig. S13. TEM and EDS mapping images of ((a) and (c)) CoO nanosheets and ((b) and (d)) Cu nanoparticles prepared by the antisolvent crystallization-based method.

Table S2. Previous reported catalysts for H_2O_2 electrochemical detection

Materials	Linear range (μM)	Sensitivity (μA mM^{-1} cm^{-2})	Detection limit (μM)	Ref.
ITO-rGO-AuNPs	25-3,000	64.1	6.65	44
Meso-C/ZnO	50-981	46.48	6.25	45
Co_3O_4/rGO/GCE	15-675	1.14	2.4	46
CuCo-Cu@CoCH	1-100 100-2,000	3,570 3,290	0.97	47
CuO/GCE	5-180	8.6	1.6	48
α-Fe_2O_3	6.6-2,500	181	1.3	49
NiO/α-Fe_2O_3	500-3,000	98.6	50	50
$CuFe_2O_4$	500-25,000	219	22	51
$CuCo_2O_4$	11-8,900	94.1	3.0	16
Cu/CoO	10-100 100-1,000	46.3 27.7	1.85	This work

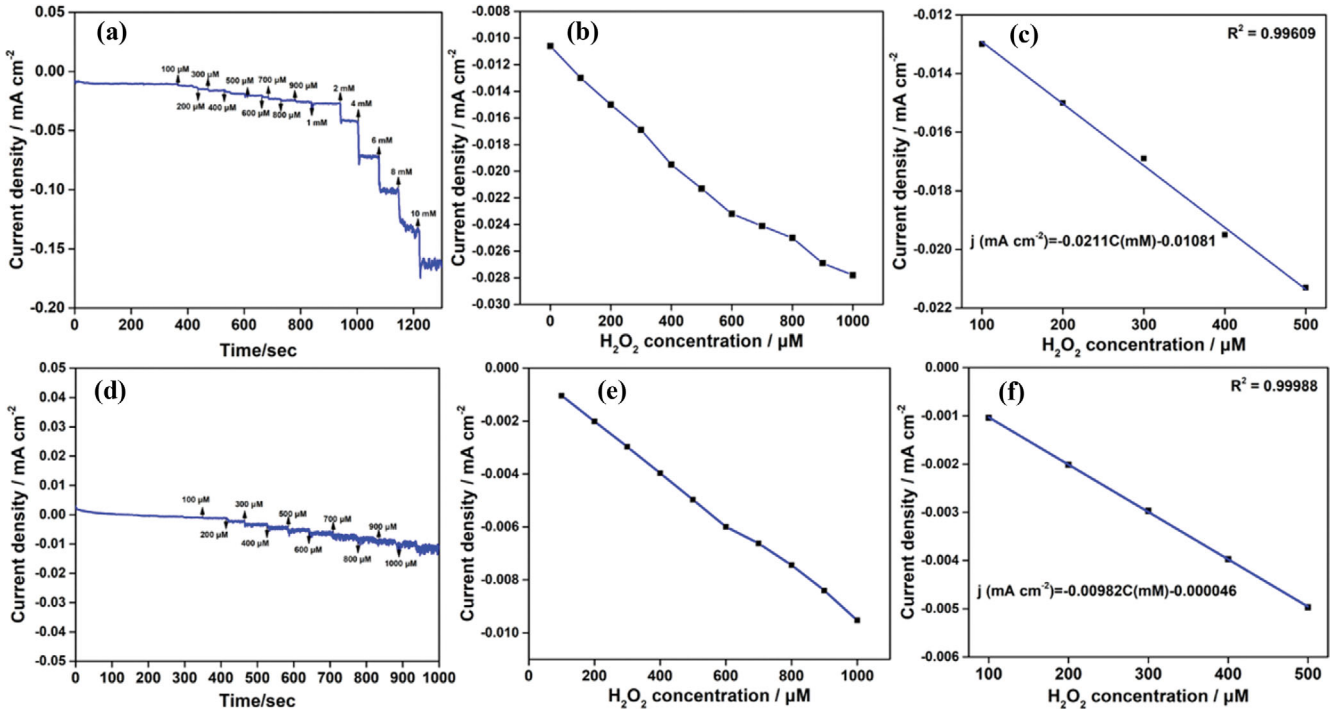

Fig. S14. Amperometric responses of the (a) CoO nanosheets and (d) Cu nanoparticles with successive additions of H_2O_2. Curves between the current density and H_2O_2 concentration of the (b) CoO nanosheets and (e) Cu nanoparticles. Linear relationship between the current density and H_2O_2 concentration in the range of 100 to 500 μM of the (c) CoO nanosheets and (f) Cu nanoparticles.